



## Co-seismic infrasound in the ionosphere over Central Europe from the M8.8 Kamchatka 2025 earthquake observed by Doppler sounding at record heights

5 Jaroslav Chum<sup>1</sup>, Zbyšek Mošna<sup>1</sup>, Jiří Baše<sup>1</sup>, Jan Zedník<sup>2</sup>, Carsten Schmidt<sup>3</sup>, Patrick Hannawald<sup>3</sup>, Jan Ruzs<sup>1</sup>, Jaroslav Urbár<sup>1</sup>, Šimon Mackovjak<sup>4</sup>

<sup>1</sup>Institute of Atmospheric Physics of the Czech Academy of Sciences, Prague, 141 00, Czech Republic

<sup>2</sup>Institute of Geophysics of the Czech Academy of Sciences, Prague, 141 00, Czech Republic

10 <sup>3</sup>German Remote Sensing Data Center of the German Aerospace Center (DLR-DFD), Oberpfaffenhofen, 82234, Germany

<sup>4</sup>Institute of Experimental Physics, Slovak Academy of Sciences, Košice, 040 01, Slovakia

*Correspondence to:* Jaroslav Chum (jachu@ufa.cas.cz)

### 15 **Abstract**

Observations of co-seismic infrasound waves and disturbances in the ionosphere recorded by continuous Doppler sounding systems (CDSS) in Czechia and Slovakia during geomagnetically quiet period and associated with the Kamchatka M8.8 earthquake on July 29, 2025, are analysed and discussed. It is shown by simultaneous ionospheric sounding by a digisonde that the co-seismic infrasound waves were detected by the CDSS at a record height of about 340 km in Czechia, more than 8000 km away from the epicentre. The Doppler shift oscillations caused by ionospheric plasma quasiperiodic movement induced by the infrasound waves had a frequency around 0.005 Hz and were observed approximately 12 min after the arrival of causative Long period surface seismic waves in Czechia. The frequency spectrum of the vertical ground surface motion that generated the infrasound waves was much broader, including more intense fluctuations with frequencies around 0.05 Hz. However, the higher frequency infrasound waves were attenuated during their propagation upward and did not reach the observation altitude, which is confirmed by numerical simulation that is in a good agreement with the CDSS observation. The numerical simulation also proves that it is necessary to consider air/plasma compression when calculating air particle velocities from the measured Doppler shift values.

### **1 Introduction**

On July 29, 2025, at 23:24:52 UT, an earthquake with a magnitude of 8.8 occurred east of the Kamchatka peninsula, about 120 km from the city of Petropavlovsk-Kamchatsky with the epicentre at 52.495°N 160.240°E and at the depth of about 35 km. The earthquake was the result of reverse faulting on the subduction zone plate interface of the Kuril-Kamchatka arc and the affected fault area was about 390×140 km (<https://earthquake.usgs.gov>). It was the third largest earthquake in the 21st century after the 2004 Sumatra and the 2011 Great Tohoku



40 earthquake. The purpose of this paper is to investigate co-seismic ionospheric perturbations associated with the Kamchatka earthquake in the ionosphere over Central Europe, about 8100 km away from the epicentre.

An investigation of atmospheric and ionospheric responses to earthquakes started already in sixties of the 20<sup>th</sup> century by the analysis of data recorded during the 1964 Alaskan earthquake  
45 (Bolt 1964; Donn and Posmentier 1964; Davies and Baker 1965). Various observation techniques have been used to detect the co-seismic perturbations in the ionosphere. One of the first and still used technique is continuous HF Doppler sounding, which allows obtaining time series of the co-seismic perturbations at reflection heights of the HF signals (Davies and Baker, 1965; Artru et al., 2004; Chum et al., 2012). An observation technique probably most widely  
50 used today are measurements of co-seismic changes in the total electron content (TEC) using the dual-frequency receivers of Global Navigation Satellite Systems (GNSS) and analysis of maps of TEC changes, which is possible due to a large number of GNSS receivers (Calais and Minster, 1995; Heki and Ping, 2005; Otsuka et al., 2006). A basic instrument for ionospheric research, the ionospheric sounder, is not frequently used to observe the co-seismic signatures  
55 in the ionosphere due the relatively low time resolution. However, multiple cusp signatures were observed in ionograms during suitable conditions, providing an important information about the vertical extent of the perturbations (Maruyama and Shinagawa, 2014; Haralambous et al., 2023). Multiple cusp signatures were also observed for the 29 July Kamchatka 2025 earthquake in the region from the western Pacific to the American west coast (Paul et al., 2026).  
60 In addition, the ionospheric sounders provide important complementary measurements to continuous HF Doppler sounding by providing an information about the reflection height of Doppler sounding signals.

It was confirmed both theoretically and experimentally that vertical motion of the ground surface, caused by seismic waves that propagate at supersonic speeds, generates infrasound  
65 waves that propagate quasi-vertically to the upper atmosphere and ionosphere and cause the co-seismic ionospheric disturbances owing to collisions between neutral particles and ionospheric plasma, detectable by techniques mentioned above (Watada et al., 2006; Rolland et al., 2011; Chum et al., 2012; Chum et al., 2016a,b; Haralambous et al., 2023). Recent reviews of the detection and analysis of ionospheric signatures generated by earthquakes and other natural hazards such as volcano eruption and tsunamis were given by Astafyeva (2019) and Wüst et al.  
70 (2026).

The GNSS TEC observations can be used to create maps displaying the co-seismic disturbances and their propagation projected into the horizontal plane at a height, in which a dense ionospheric plasma occurs and/or at a height in which perturbations are assumed  
75 (Astafyeva and Heki, 2009; Liu et al., 2011; Zettergren and Snively, 2019). The GNSS TEC values and their changes represent integral values along the line of sight to the GNSS satellite

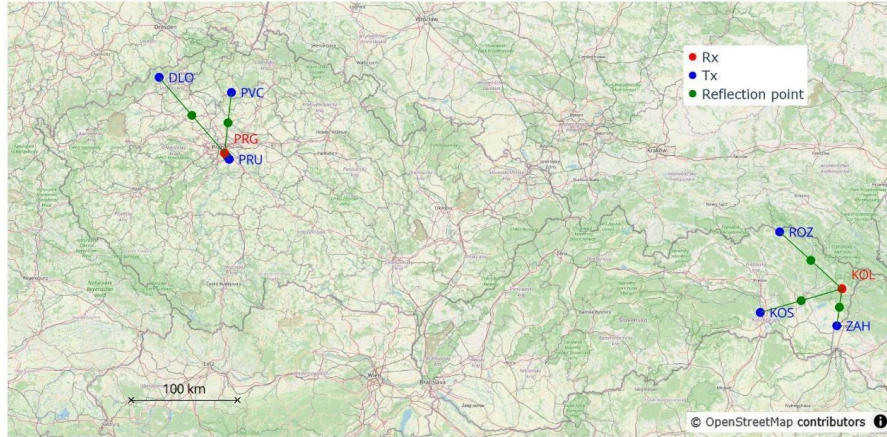


and do not provide information about the phase and amplitude of waves in a specific/known altitude. However, it is possible to do a three-dimensional reconstruction (tomography) of ionospheric perturbations using a dense network of GNSS receivers (Song et al., 2025),  
80 nevertheless, the vertical and time resolution needed for a successful reconstruction is relatively low, about 30 km and 2 min, respectively.

On the other hand, continuous HF Doppler sounding operating close to an ionospheric sounder can provide the waveform of the co-seismic perturbation, infrasound wave, at a specific altitude (given by the sounding frequency and determined from ionograms) with a high time  
85 resolution (up to several seconds). So far, the co-seismic infrasound waves were observed using Doppler sounding at altitudes around 200 km or lower in Central Europe (Chum et al., 2012; Chum et al., 2016a; Haralambous et al., 2023) and, to the best of our knowledge, also in the world. In this paper we present an observation of co-seismic infrasound by Doppler sounding in record breaking height of about 340 km. It is also shown that only waves with longer periods  
90 were able to reach such altitudes; the shorter periods were attenuated below. The observation is consistent with numerical simulation of infrasound propagation.

## 2 Data and methods

The Czech multipoint Continuous Doppler Sounding System (CDSS) operates at  
95 frequencies of 3.59, 4.65 and 7.04 MHz (Laštovička and Chum, 2017). Its main application is monitoring and analysis of medium-scale ionospheric travelling disturbances associated with atmospheric gravity waves (Chum et al., 2021), but due to its high time resolution (several seconds) it can also be used to detect and analyse co-seismic infrasound and transient phenomena such as sudden frequency deviations caused by X-ray and extreme ultraviolet  
100 radiation produced during solar flares and sudden storm commencements (Chum et al., 2016a,b; Chum et al., 2018a,b, Kikuchi et al., 2021, 2022). There are three transmitting sites (Tx), labelled PVC, PRU and DLO in Figure 1, which operate at all three frequencies in Czechia. The receiver (Rx) used in this study is located in Prague (50.04°N, 14.48°E), about 8150 km away from the epicentre and about 7 km away from the digisonde DPS-4D in Pruhonice, PQ052  
105 (Reinisch et al., 2005), which is about 200 m away from the PRU Tx site. To exclude a local effect, data from CDSS (operating at 3.59 MHz) installed in Eastern Slovakia with receiver in Kolonica (48.93°N, 22.27°E), about 8060 km away from the epicentre and marked KOL in Figure 1, are also investigated. The Slovak transmitters are labelled KOS, ROZ and ZAH.



110

**Fig. 1** Distribution of CDSS transmitters (Tx, blue dots) and receivers (Rx, red dots) in Czechia and Slovakia. Digisonde DPS-4D is collocated with the Tx in Pruhonice (PRU), and the seismometer is collocated with the Tx in Panská Ves (PVC) in Czechia.

115

Reflection points of the Doppler signals, if projected to the ground, are assumed in the midpoints between each transmitter and receiver (Figure 1). The half distances between the transmitters and receiver (few tens of km) are much smaller than the reflection heights (more than 300 km in this case). So, the sounding is quasi-vertical, which means that azimuthal angles  $\alpha$  of sounding radio waves are small,  $\cos(\alpha) \approx 1$ , and the sounding radio waves (ordinary mode) reflect at heights where their frequency matches the local plasma frequency. If the ionospheric plasma in the reflection region moves (radially relative to the CDSS) or if the electron density changes, then the reflected radio wave experiences a Doppler shift. Assuming a sharp electron density gradient, the radial/vertical plasma velocity  $w_p$  can be computed from the obtained Doppler shift  $f_D$  as

120

$$125 \quad w_p = -f_D \cdot \frac{c}{2f_0} \quad , \quad (1)$$

where  $c$  is the speed of light and  $f_0$  is the frequency of the sounding radio wave (Davies et al., 1962; Jacobs and Watanabe, 1966).

130

In the ionospheric F region, plasma is fully magnetized and moves freely only along magnetic field lines. Therefore, the vertical component of plasma motion  $w_p$  induced by vertically moving air particles with velocity  $w$  due to the infrasound waves is given by

$$w_p = w \cdot \sin^2(I) \quad , \quad (2)$$

where  $I$  is the inclination of the magnetic field ( $\sim 66^\circ$  in Czechia).

135

Because the plasma frequency and refractive index of the radio waves depend on the electron density, the Doppler shift is related to the electron density changes, especially at the region of reflection. Several authors (e.g., Sutcliffe and Poole, 1989 and references therein) used the



equation of continuity and argued that alternating plasma compression caused by compressional magnetohydrodynamic waves should also contribute to the Doppler shift. However, the experimental results were inconclusive in the case of magnetohydrodynamic waves. Chum et al. (2012, 2016a) applied their approach and using the equation of continuity derived equation  
140 (3) which relates the observed Doppler shift  $f_D$  with the air particle vertical velocity  $w$  induced by vertically propagating infrasound waves.

$$w = -f_D \cdot \frac{c}{2f_0 \sin^2(\theta)} \cdot \frac{\frac{\partial N}{\partial z}}{\sqrt{(\frac{\partial N}{\partial z})^2 + (N \frac{2\pi f_{IS}}{c_s})^2}}, \quad (3)$$

where  $f_{IS}$  is the infrasound frequency,  $c_s$  is the sound speed at the reflection height,  $N$  is the electron density and  $\partial N/\partial z$  is the vertical gradient of the electron density at the reflection height  
145 estimated from the true height profile of the plasma frequency  $f_p$  obtained from the ionogram, e.g., by SAO Explorer software (Reinisch et al. 2005). A definition of plasma frequency  $f_p$  is used to relate  $f_p$  and  $N$ . The term  $N \cdot (2\pi f_{IS})/c_s$  in the denominator of equation (3) results from the air/plasma compression due to the infrasound waves. See Chum et al., (2016a) for more details and derivation. Note that if  $(\partial N/\partial z)^2 \gg (N \cdot (2\pi f_{IS})/c_s)^2$ , then equation (3) reduces to  
150 equation (1) with usage of equation (2). Chum et al. (2012, 2016a) also showed that not considering the compressional term  $N \cdot (2\pi f_{IS})/c_s$  can lead to results that are inconsistent with energy conservation for specific cases of the co-seismic infrasound observations.

The near surface air particle vertical oscillation velocities  $w_0$  are determined by the vertical velocity of Earth surface motion,  $v_z$ , (Watada et al., 2006), which is measured by a seismometer  
155 co-located with PVC transmitter in the Panská Ves observatory (50.53° N, 14.57° E). The infrasound waves generated by seismic waves propagating far away from the epicentre propagate nearly vertically owing to the supersonic speed of seismic waves. Specifically, the expected zenith angle  $\delta$  of the generated infrasound waves above the surface is given by equation (4)

$$160 \quad \sin(\delta) = \frac{c_{s0}}{c_G}, \quad (4)$$

where  $c_{s0}$  is the sound speed above the ground and  $c_G$  is the speed of seismic waves (Rolland et al., 2011; Chum et al., 2016a). As  $c_G$  is about 10 times larger than  $c_{s0}$ , the deviation of initial infrasound wave vector from the zenith direction is around 6°.

The observed time delays between the ground surface velocities and co-seismic infrasound  
165 waves recorded by the CDSS are also compared with ray tracing simulation, including attenuation along the ray tracing trajectories due to the viscosity and thermal conductivity. The air temperature and neutral species densities at specific locations and time needed for sound speed calculation and attenuation estimate are obtained from the NRLMSIS model (Emmert *et al.* 2020) with a possibility to include also neutral winds using the horizontal wind model  
170 HWM14 (Drob *et al.* 2015). A more detailed description of the ray tracing software features



can be found in Chum et al. (2023) and references therein. In addition, one-dimensional full-wave simulation of vertical infrasound propagation based on the numerical solution of the equation of continuity, the equation of motion/momentum (Navier-Stokes equation) and the heat equation using an implicit finite difference method, including non-linear terms, is performed to investigate the expected evolution of the wave spectrum with height and to estimate the expected air particle velocities at specific heights (see Chum et al., 2016b, 2018a for a more detailed description of the simulation method).

We also check other available measurements that could provide information on atmospheric waves at specific altitudes, such as airglow measurements of the hydroxyl (OH) layer in the mesopause region around 86 km using the OH temperature measurements by the Ground-based Infrared P-branch Spectrometer (GRIPS) and wave detection by the Fast Airglow Imager (FAIM) installed in Panská Ves (Schmidt et al., 2013; Hannawald et al., 2016). Both airglow instruments were setup to observe the OH layer directly below the reflection point of the CDSS (the green point between PVC and PRG in Figure 1). In addition, electron density measurements by Swarm satellites are investigated. There are three Swarm satellites launched to nearly polar orbits. The satellites A and C are flying at ~465 km altitude, while Swarm B orbits at ~520 km (Friis-Christensen et al., 2008).

The indices of geomagnetic activity, searched to verify the geomagnetic activity, are taken from the World Data Center for Geomagnetism, Kyoto.

### 3 Results

Despite the maximum of solar cycle 25, the M8.8 Kamchatka earthquake occurred during a period when ionosphere was not significantly disturbed by space weather drivers. There were no M or X-class flares and neither strong geoeffective coronal mass ejections nor high-speed streams of solar wind plasma. Therefore, the geomagnetic activity was very low, with the following values of geomagnetic indices: Dst~12 nT and Kp~2. The conditions were therefore favourable to study the ionospheric response to acoustic-gravity waves of known origin and amplitude propagating from below. As the space weather influence was minimal, the interpretation of the origin of the detected ionospheric variations is relatively straightforward.

Figure 2a shows the vertical velocity  $v_z$  of ground surface motion measured in Panská Ves, Czechia, in the time interval of 70 min from the onset of the earthquake on July 29, 2025, at 23:24:52 UT. A detection of the Primary body (P) waves in Panská Ves started after 23:36 UT and continued until about 23:40 UT, with relatively small amplitudes in  $v_z$  (less than 0.1 mm/s). Secondary shear body waves once reflected from the Earth's surface (SS) were detected in the vertical component after 23:50 UT and had similar amplitudes as the P waves. The surface waves reached much larger amplitudes and were observed on July 30, 2025, approximately between 00:00 and 00:20 UT. Specifically, Long period surface (L) waves with amplitudes



reaching up to around 0.4 mm/s were observed approximately between 00:00 and 00:10 UT, and Rayleigh (R) waves with shorter periods and amplitude exceeding 1 mm/s were recorded  
210 between 00:10 and 00:20 UT.

Following the activity of seismic waves, fluctuations in Doppler shifts  $f_D$  with a frequency about 0.005 Hz (period about 200 s) were observed in the CDSS records around 00:20 UT at sounding frequencies 4.65 and 3.59 MHz in Czechia (sounding frequency 7.04 MHz was above the maximum plasma frequency in the ionosphere, the critical frequency, so the 7.04 MHz signals did not reflect from the ionosphere). There were no time delays (within the time resolution) between the infrasound signals on individual sounding paths (Tx-Rx pairs), so the signals from all three transmitters were averaged at each time point. The values of the observed Doppler shifts were converted to the vertical plasma velocities  $w_p$  and vertical air particle velocities  $w$  using equations (1) and (3), respectively, and after filtering out longer period  
215 fluctuations of different origin (larger than about 5 min) displayed in Figure 2b (4.65 MHz) and Figure 2c (3.59 MHz). The  $w_p$  and  $w$  velocities obtained from the Czech CDSS are by blue and red, respectively. The  $w_p$  velocity measured by the CDSS in Slovakia is shown by green dashed line in Figure 2c (the  $w$  is not calculated because of the absence of a nearby ionosonde that could provide the  $\partial N/\partial z$  gradient). The signal (dominant wave packet) observed by the Czech  
220 CDSS at 3.59 MHz precedes by about 40 seconds the signal recorded at 4.65 MHz. The  $w_p$  amplitudes (equation 1) reached about 9 and 15 m/s at 3.59 and 4.65 MHz, respectively, and the  $w$  amplitudes (equation 3) were about 5.5 and 4.8 m/s at 3.59 and 4.65 MHz. The  $w_p$  amplitudes were larger at 4.65 MHz than at 3.59 MHz, whereas the  $w$  amplitudes were higher for 3.59 MHz. The reason for this is a difference in the values of electron density gradient,  
225  $\partial N/\partial z$ , at reflection heights for 3.59 and 4.65 MHz waves, as will be shown later.

It is reminded that application of equation (3) also requires a knowledge of a dominant frequency at the reflection height to calculate  $w$ . An insight in a spectral content of the observed waves and their evolution with time is shown in dynamic spectra displayed in Figure 3. It is important to note that the seismic wave packet labelled L (Figure 2a and Figure 3a) contains a  
235 very broad frequency spectrum, including frequencies around 0.005 Hz, which are detected also in the Doppler shift records (Figures 3b and 3c), approximately 11-13 min later. The frequency of 0.005 Hz was used to calculate  $w$  shown in Figure 2b and 2c.

The reflection heights of the ordinary mode of the sounding radio waves with frequencies 3.59 and 4.65 MHz are about 305 and 340 km, respectively, as shows the height profile of  
240 plasma frequency (true height profile) obtained from the ionogram recorded in Pruhonice on July 30 at 00:25 UT, which is displayed in Figure 4. The average reflection heights for the 3.59 and 4.65 MHz waves in the time interval from 00:10 to 00:30 UT obtained from a sequence of ionograms are 303 and 336 km, respectively. Figure 4 also shows the estimated inverse of the



245 plasma density gradients at the reflection heights, from which the electron density gradient  
 $\partial N/\partial z$  is obtained using the definition of plasma frequency  $f_p$ . The obtained values are  $\partial N/\partial z =$   
3.56·10<sup>6</sup> and 2.75·10<sup>6</sup> m<sup>-4</sup> at the reflection heights of 3.59 and 4.65 MHz waves, respectively.  
These values were used to calculate vertical air particle velocities  $w$  plotted in Figures 2b and  
2c.

250 To verify that the observed time delays correspond to the propagation of infrasound waves,  
which are a probable cause of the ionospheric disturbances, we performed a ray tracing  
simulation. Figure 5a shows the simulated propagation time (orange) and sound speed (black)  
of the infrasound waves launched with the zenith angle 6° from the Panská Ves location on July  
30, 2025 at 00:06 UT. The propagation times to altitudes 305 and 340 km are 680 and 724 s,  
respectively. The sound speeds at these altitudes are 807 and 837 m/s, respectively. The  
255 modelled propagation times are consistent with the observed time delays between the 0.005 Hz  
signal recorded on the ground by the seismometer and in the ionosphere by the CDSS at about  
305 and 340 km altitudes.

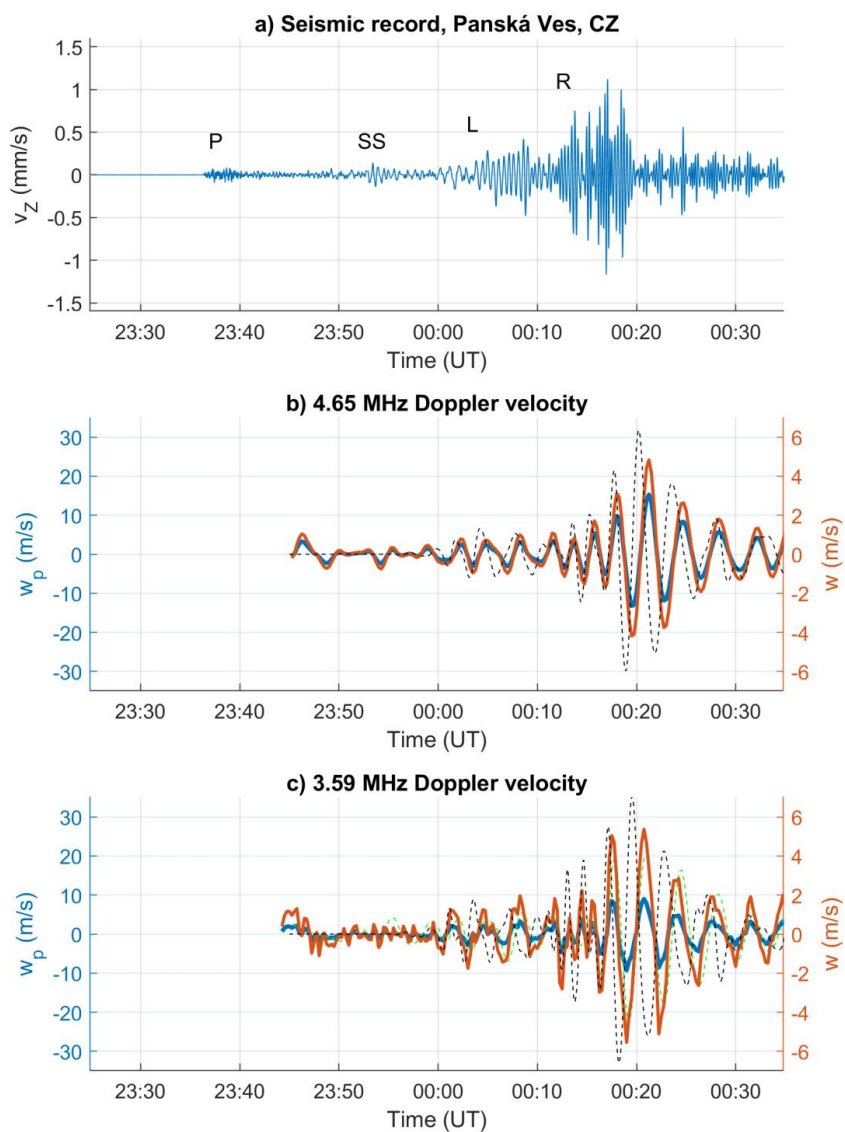


**Fig. 2** a) Vertical velocity  $v_z$  of the ground surface motion in Panská Ves on the night of July 29 to 30, 2025 b) and c) Vertical velocity of plasma motion  $w_p$  directly obtained from the observed Doppler shift (blue) and the calculated vertical velocity of air particle oscillation  $w$  (red) for measurements at  $f=4.65$  and  $3.59$  MHz, respectively. Black dashed lines show the simulated vertical air particle oscillation velocity at altitudes 340 and 305 km, respectively,



265 scaled to the right axis. The green line in the plot c) displays the  $w_p$  velocity obtained in Slovakia.

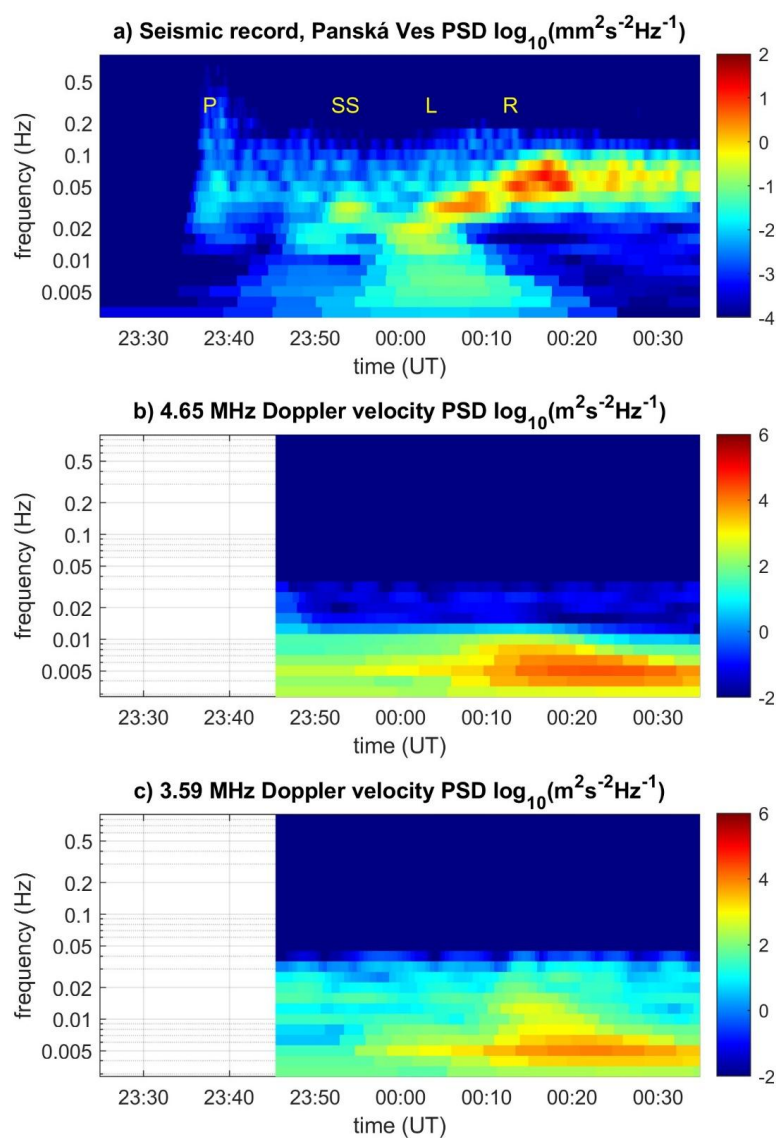


**Fig. 3** Dynamic spectra (power spectral densities) of vertical velocity  $v_z$  of the ground surface motion on the night of July 29 to 30, 2025 (a), and of the Doppler shifts measured at  $f=4.65$  MHz (b) and 3.59 MHz (c). The dynamic spectra correspond to signals presented in Figure 2.

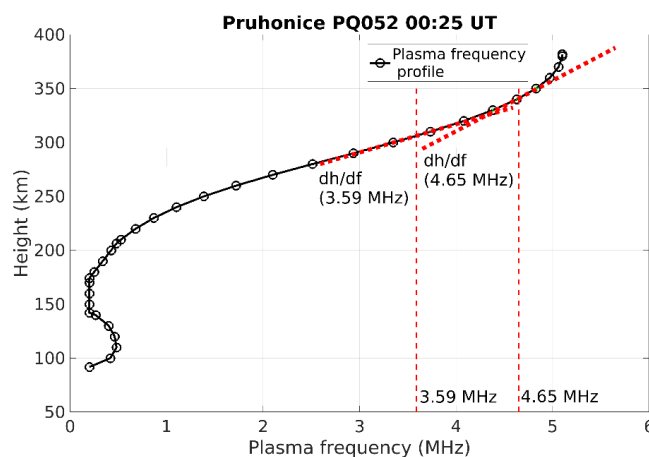


270

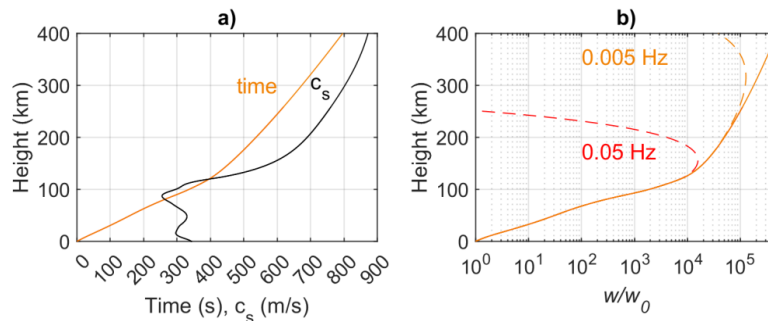
Dashed lines in Figure 5b show the ratios  $w/w_0$ , which represent the expected/simulated vertical air particle velocities  $w$  at a specific altitude normalized by their near surface value  $w_0$ , including the frequency dependent attenuation along the ray trajectories for infrasound frequencies 0.05 (red) and 0.005 (orange) Hz. The solid line displays the expected ratio for an unrealistic lossless (infra)sound plane wave propagation for which the infrasound power flux is conserved. It means that the quantity  $c_s \rho w^2$  is constant, where  $\rho$  is the air density, decreasing exponentially with height (obtained from the NRLMSIS model). Figure 5b shows that waves with a frequency of 0.05 Hz begin to be significantly attenuated above an altitude of approximately 150 km. On the other hand, the 0.005 Hz waves can reach the height of 300 km without a significant attenuation. The ratio  $w/w_0$  (normalized velocity  $w$ ) for 0.005 Hz waves at the observation heights 305 and 340 km is  $1.26 \cdot 10^5$  and  $1.19 \cdot 10^5$ , respectively. For idealized lossless propagation it is  $1.89 \cdot 10^5$  and  $2.74 \cdot 10^5$ , respectively, at these heights.

275

280



285 **Fig. 4** True height profile of plasma frequency derived from the measurements by the digisonde located in Průhonice, PQ052, on July 30, 2025 at 00:25 UT. The CDSS sounding frequencies 3.59 and 4.65 MHz and the vertical plasma density gradients are marked by red.



290 **Fig. 5** a) Simulated infrasound propagation time (orange) and sound speed (black) as a function of height. b) Simulated vertical air particle oscillation velocities  $w$  normalized to the initial value  $w_0$  above the ground surface for frequencies 0.05 Hz (red) and 0.005 Hz (orange). The solid orange line represents an idealized case of lossless propagation of a plane wave.

295 It is important to stress that a comparison of the observed values  $w$  ( $w_p$ ) displayed in Figure 2 with the simulated values  $w$  shown in Figure 5b is not straightforward. The reason is that the calculated normalized values  $w/w_0$  correspond to monochromatic waves. The wave attenuation with height strongly depends on the wave frequency. The higher frequency, the lower is the altitude at which the wave energy dissipates (Figure 5b). Figure 3a shows that the seismic wave packet L contained a very wide range of frequencies and therefore generated infrasound in a broad frequency spectrum. However, only the waves corresponding to frequencies around 0.005 Hz - a small energy fraction could reach the heights above 300 km, where the induced plasma fluctuations were detected by the CDSS. Therefore, for the wave packet L it makes no sense to compare the observed amplitudes  $w$  ( $w_p$ ) normalized by the  $v_z$  amplitude (Figure 2) with the simulated ratio  $w/w_0$  (Figure 5b).

305 To compare the observed amplitudes obtained from the CDSS measurements with the expected values, we performed full wave one-dimensional numerical simulation of infrasound propagation in the vertical direction, started with initial perturbations above the Earth's surface defined by the vertical motion of the ground surface,  $w_0=v_z$ . The assumption of this initial perturbation is based on theoretical work (Watada et al., 2006) and was successfully applied in previous studies (Chum et al., 2018a and references therein). The  $w$  values obtained by the full-wave numerical simulation at the heights 305 and 340 km are plotted in Figure 2c and 2b, respectively, by the dashed black lines. The values are scaled to the right ( $w$ ) axis and the maximum amplitudes are about 6.8 m/s at 305 km and 6.2 at 340 km. It means that they are about 30% larger than the  $w$  values estimated from the measurement. The main fluctuations of the simulated waveforms occur at approximately similar times as the  $w$  ( $w_p$ ) values derived from the observed Doppler shifts and have also similar frequencies. Therefore, the simulation



agrees reasonably well with the observation. It should be noted in this respect, that the real  
trajectory of infrasound waves will be somewhat longer than the vertical distance due to the  
320 non-zero zenith angle of propagation and due to the neutral winds, which may affect the  
trajectory. Consequently, the location of the seismometer in Panská Ves (PVC in Figure 1) may  
not be the exact source location of the waves that reach the observation points.

Figure 6 shows the height evolution of the air particle velocity fluctuation spectra obtained  
by the one-dimensional full-wave numerical simulation started with the fluctuations defined by  
325 the seismic record,  $w_0=v_z$ . The power spectral densities of  $w$  are normalized to their maximum  
value above the ground surface and their colour-coded common logarithm is displayed in Figure  
6. The height-dependent spectra in Figure 6 confirm that only waves with the lowest frequencies  
(about 0.005 Hz) can reach the observation altitudes, although they carry just a small fraction  
of the total wave energy at altitudes lower than about 200 km.

330

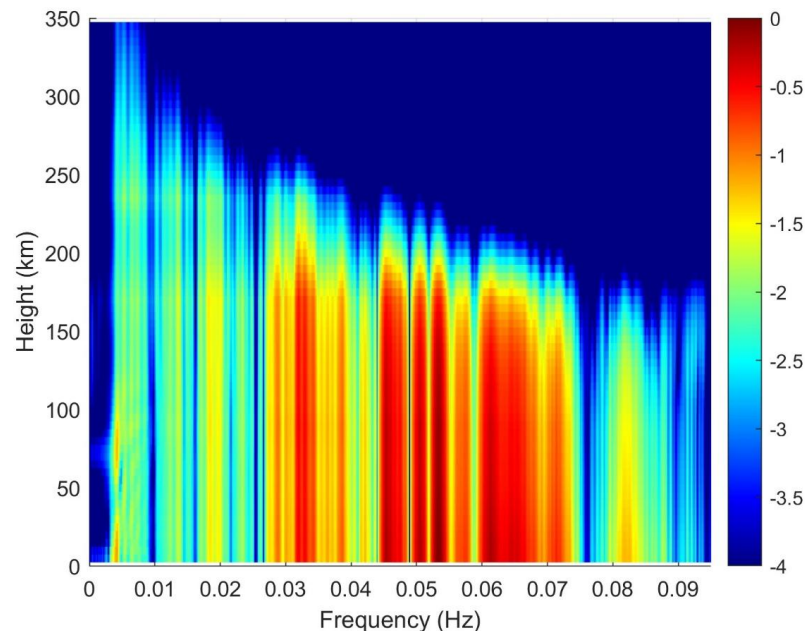
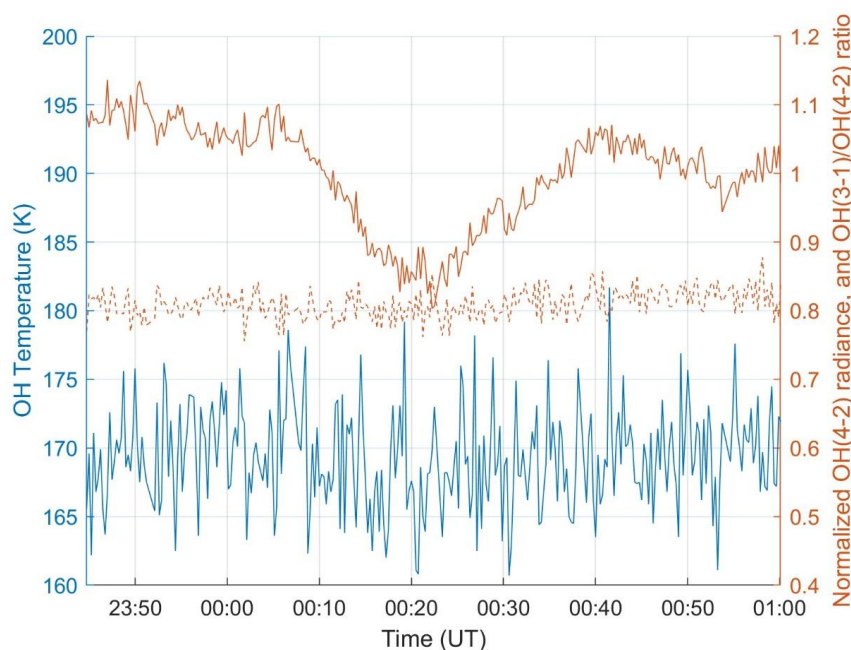


**Fig. 6** Expected power spectral densities (colour coded common logarithm) at different altitudes, normalized to the ground level.

335 We also investigated the measurements of OH airglow emissions originating from an about  
10 km thick layer around 86 km, which may be modulated by atmospheric waves (Snively,  
2013; Wüst et al., 2023). Figure 7 shows that no significant changes in the OH temperature  
related to the infrasound waves were detected over Czechia, despite intensity drops in the used



OH(3-1)- and OH(4-2)-Q-branches, approximately in the interval from 00:05 to 00:35 UT,  
340 which roughly coincides with the occurrence of the co-seismic infrasound waves. On the one  
hand the ratio of these two emissions serves as a cloud indicator (OH(3-1)-Q at 1.505  $\mu\text{m}$  is  
more strongly attenuated by water and ice droplets compared to OH(4-2)-Q at 1.585  $\mu\text{m}$ ). On  
the other hand, both emissions originate at slightly different centroid altitudes, separated by  
0.5-1.0 km (e.g., von Savigny et al., 2012). Atmospheric waves with short vertical wavelengths  
345 passing through the OH layer will therefore leave a clear signature in the OH(3-1)/OH(4-2)-  
ratio, while waves with large vertical wavelengths (affecting both emissions at the same time)  
will not (Schmidt et al., 2018). While this drop in intensity without a significant change in the  
OH(3-1)/OH(4-2)-ratio indicates the presence of an atmospheric structure with large vertical  
scales, the OH imager (FAIM) shows the presence of a varying number of small clouds in the  
350 fields of view of both instruments at this time. The passage of clouds also prevented a potential  
detection of waves in the OH airglow images. In addition, a similar drop in OH intensities were  
not observed in other European stations equipped with the OH imager and spectrometer in this  
time interval. Thus, the co-seismic origin of the intensity drop is questionable. The time  
resolution of OH temperature measurement by GRIPS is 15 s. This sampling frequency does  
355 not allow for the analysis/detection of waves with a dominant frequency of approximately  
0.05 Hz, which is expected at the height of the OH layer (Figure 6). The waves with frequency  
around 0.005 Hz were not detected in the OH temperature time series at the expected time  
(around 00:10 UT on July 29, 2025) using the continuous Wavelet Transform (not shown).





360 **Fig. 7** OH temperature (blue) and OH(4-2) radiance (solid red) on the night of July 29 to 30,  
2025. The nearly constant ratio (dashed red) between OH(3-1)- and OH(4-2)-emissions  
indicates a structure with large vertical wavelengths/scales being associated with the drop in  
intensity. See text for further details.

365 There were no passes of the Swarm satellites over Europe in the investigated time interval  
(approximately from 23:45 July 29 to 00:45 July 30). The closest pass over East Romania was  
on July 30 after 01:00 UT. It should be noted in this respect that a probability of detecting  
atmospheric waves at the altitude of the satellite orbit is relatively small due to the attenuation  
of the waves. The co-seismic signatures related to the M8.8 Kamchatka earthquake were not  
370 not detected by the Swarm satellites over East Asia, at much closer distances from the epicentre  
(Paul et al., 2025).

#### 4 Discussion and Conclusions

The simulated air particle vertical velocities  $w$  shown in Figure 2 by black dashed lines are  
375 about 30% larger than the values obtained from observation using equation (3). This is a  
reasonable agreement considering the uncertainties in determination of  $\partial N/\partial z$  gradients (around  
10%). Importantly, it is reasonable to expect that the observed  $w$  are smaller, than the simulated  
values for several reasons. First, the simulation is based on the plane wave propagation (one-  
dimensional simulation) and does not take into account a possible divergence of infrasound ray  
380 trajectories, and therefore does not consider a decrease of the infrasound power flux due to the  
geometrical spreading of the waves. Second, the simulation only considers attenuation due to  
the viscosity and thermal conductivity (Chum et al., 2016b), but does not simulate other  
possible losses, for example, rotational relaxation losses, turbulent losses etc. (Bass et al., 1984).  
Third, the actual trajectory of infrasound waves may be longer than the pure vertical distance,  
385 and consequently the attenuation larger, due to the non-zero zenith angle and due to the neutral  
winds. It is useful to stress that both the plasma velocities  $w_p$  and the air particle velocities  
obtained directly from  $w_p$  by using equation (2), without including the compressional term, give  
values roughly 100% larger than the simulated values, which is highly improbable for the  
reasons mentioned above, and indicates the need to use the compressional term in the  
390 quantitative analysis of infrasound amplitudes using Doppler shift measurements.

The observed time delay of about 12 min between the 0.005 Hz waves in the seismic record  
and the waves of the same frequency in the Doppler shift (air particle velocity fluctuations) is  
consistent with the numerical simulation of infrasound propagating in the (quasi)vertical  
direction. In addition, the 3.59 MHz CDSS in Czechia detects the co-seismic signal  
395 approximately 40 s sooner than the 4.65 MHz CDSS, the signal of which is reflected at the  
altitude about 35 km higher.



The Slovak 3.59 MHz CDSS detects the co-seismic infrasound waves at a similar time as the Czech CDSS, with a phase shift locating the main fluctuations roughly between the 3.59 and 4.65 MHz signals in Czechia (Figure 2c). This indicates that the reflection height for the 3.59 MHz radio waves is somewhat larger in Slovakia than in Czechia, considering (quasi)vertical propagation of infrasound and similar horizontal distances from the epicentre (about 8150 km the Czech CDSS and about 8060 km the Slovak CDSS). The vertical plasma velocities  $w_p$  obtained without considering the compressional term (equation 1) are about 100% higher in Slovakia than in Czechia. It is reminded that there is no nearby ionosonde in Slovakia that would provide reliable  $\partial N/\partial z$  values for calculating the more realistic velocities  $w$  using equation (3). However, if we assume that the air particle velocities  $w$  are approximately the same over Czechia and Slovakia, then it follows from equation (3) that the electron density gradient  $\partial N/\partial z$  at the corresponding reflection heights of 3.59 MHz signals must be smaller in Slovakia, than in Czechia. This is consistent with the higher reflection height in Slovakia deduced from the timing mentioned above (note that  $\partial N/\partial z$  usually decreases with height in the F2 layer, when approaching the peak of the layer).

Unlike the previous observation of co-seismic infrasound waves by CDSS in Czechia, triggered by strong earthquakes, namely M9.0 Tohoku 2011, M7.8 Nepal 2015, and M7.7 Turkey 2023 earthquakes, when the shape and spectral content of the wave packets in the co-seismic Doppler shift fluctuations was very similar to that recorded in the vertical velocity  $v_z$  of ground surface motion (Chum et al., 2012; Chum et al., 2016a; Haralambous et al., 2023), the spectral content of the detected co-seismic ionospheric waves associated with the M8.8 Kamchatka earthquake differed significantly from  $v_z$ . The main reason for that is the high altitude of observation and filtering out of waves with higher frequencies during the infrasound propagation to such a high altitude, including waves with frequencies that are dominant at lower altitudes.

It should be stressed that the change of the wave packet shape and absence of waves with higher frequencies at the CDSS observation height in this case is not caused by nonlinear effects, which are a consequence of large amplitude of infrasound waves in the upper atmosphere that may occur for sufficiently strong initial perturbations  $w_0=v_z$  (Chum et al., 2016b; Chum et al., 2018a), but purely by filtering out of waves with higher frequencies due to the wave attenuation, which strongly depends on wave frequency. Unlike the case of nonlinear effects (Chum et al., 2016b), a nonlinear simulation started with an initial perturbation  $w_0=v_z/10$  provides in this case practically the same wave packet (spectral content) at the observation altitude, only with  $\sim 0.1$  amplitude, when compared with the simulation started for  $w_0=v_z$ .

The co-seismic infrasound waves have never been observed at  $\sim 340$  km height by the CDSS in Czechia before. All the previous Czech observations of co-seismic infrasound were from an



altitude range approximately 150-220 km. To the best of our knowledge, we are not aware of  
any Doppler observation of co-seismic infrasound in such a height in other countries. It is  
435 reminded that although TEC perturbations detected by GNSS receivers are usually mapped to  
the peak of F2 layer, they are usually observed with a 8-9 min delay with respect to the seismic  
record (Astafyeva et al., 2019; Wüst et al., 2026 and references therein), which indicates  
dominant perturbations at ~250 km or below when considering the expected sound speed height  
profile (e.g., Figure 5a). There is actually no direct information about the altitude of the TEC  
440 disturbance due to the height integrated nature of the TEC GNSS measurements. On the other  
hand, ionospheric disturbances associated with tsunami waves were with a high probability  
detected at the altitudes above 400 km by Low Earth Orbit satellites (Yang et al., 2022; Alfonsi  
et al., 2024), but these perturbations are related to the gravity waves, rather than to infrasound.  
Therefore, the detection of infrasound waves in the ionosphere by the CDSS at the height of  
445 around 340 km and about 12 min after the arrival of causative Long period surface seismic  
waves is a unique observation, which experimentally proves that low frequency infrasound  
waves can reach such a high altitude.

#### Appendix A: List of abbreviations

450 CDSS continuous Doppler sounding system  
GNSS global navigation satellite system  
OH hydroxyl  
Rx receiver  
TEC total electron content  
455 Tx transmitter  
UT universal time

#### Data availability

Th CDSS data are available at the <http://datacenter.ufa.cas.cz/> (spectrogram archive), or more  
460 specifically, including the time series related to Kamchatka earthquake, using the link  
[http://datacenter.ufa.cas.cz/publicdata/archive/three\\_paths/](http://datacenter.ufa.cas.cz/publicdata/archive/three_paths/). The digisonde data can be found at  
<https://giro.uml.edu/ionoweb/> (select PQ052 station). The seismic data are available, e.g., at  
<https://www.fdsn.org/networks/detail/CZ/>. The OH airglow data can be obtained at  
<https://zenodo.org/records/18788838>.

465

#### Authors contribution

JC designed the article, wrote the texts and performed most of the analysis. ZM analysed the  
ionograms, JB engineered and maintained the CDSS, JZ provided the seismic data and their



470 analysis, CS was responsible for the OH temperature measurements, PH was responsible for  
the OH imager data, JR helped with Figures, JU checked the Swarm data, and SM was  
responsible for the CDSS in Slovakia. All authors read and approved the submitted version.

#### Competing Interest

475 The authors declare that they have no conflict of interest.

#### Acknowledgement

Community Coordinated Modeling Center at Goddard Space Flight Center and their publicly  
available simulation services (<https://ccmc.gsfc.nasa.gov>) are acknowledged for the NRLMSIS  
480 model used in our ray tracing code and full wave numerical simulation. The World Data Center  
for Geomagnetism, Kyoto (<https://wdc.kugi.kyoto-u.ac.jp/>) is acknowledged for the  
geomagnetic indices.

#### Funding

485 The support by the ESA project Swarm QUID-REGIS ESA, contract No. 4000143632/24/I-EB  
is acknowledged.

#### References

- Alfonsi, L., Cesaroni, C., Hernandez-Pajares, M., Astafyeva, E., Bufferal, S., Elias, P., et al.  
490 (2024). Ionospheric response to the 2020 Samos earthquake and tsunamis. *Earth Planets  
and Space*, 76(1), 13. <https://doi.org/10.1186/s40623-023-01940-2>
- Artru J, Farges T, Lognonné P (2004) Acoustic waves generated from seismic surface waves:  
propagation properties determined from Doppler sounding observations and normal-mode  
modeling. *Geophys J Int* 158:1067–1077
- 495 Astafyeva, E.: Ionospheric detection of natural hazards. *Reviews of Geophysics* 57(4),  
1265–1288 (2019) <https://doi.org/10.1029/2019RG000668>
- Astafyeva, E., & Heki, K. (2009). Dependence of waveform of near-field co-seismic  
ionospheric disturbances on focal mechanisms. *Earth Planets Space*, 61(7), 939–943.  
<https://doi.org/10.1186/bf03353206>
- 500 Bass H, Sutherland ELC, Piercy J, Evans L (1984), Absorption of sound by the atmosphere,  
in *Physical Acoustics*, Vol. XVII, Chap. 3., edited by W. P. Mason and R. N. Thurston,  
pp.145-232, Academic Press, Inc
- Bolt BA, (1964) Seismic air waves from the great 1964 Alaskan earthquake. *Nature*  
202:1095-1096. doi:10.1038/2021095a0



- 505 Calais, E., and J. B. Minster (1995), GPS detection of ionospheric perturbations following the January 17, 1994, Northridge earthquake, *Geophys. Res. Lett.*, 22, 1045–1048, doi:10.1029/95GL00168.
- Chum, J., F. Hruska, J. Zednik, and J. Lastovicka (2012), Ionospheric disturbances (infrasound waves) over the Czech Republic excited by the 2011 Tohoku earthquake, *J. Geophys. Res.*, 117, A08319, doi:10.1029/2012JA017767.
- 510 Chum J., Y.-J. Liu, J. Laštovička, J. Fišer, Z. Mošna, J. Baše, Y.Y. Sun (2016a), Ionospheric signatures of the April 25, 2015 Nepal earthquake and the relative role of compression and advection for Doppler sounding of infrasound in the ionosphere, *Earth, Planets and Space*, 68:24, DOI 10.1186/s40623-016-0401-9
- 515 Chum, J., M. A. Cabrera, Z. Mošna, M. Fagre, J. Baše, and J. Fišer (2016b), Nonlinear acoustic waves in the viscous thermosphere and ionosphere above earthquake, *J. Geophys. Res. Space Physics*, 121, doi:10.1002/2016JA023450.
- Chum, J., J.-Y. Liu, K. Podolská, T. Šindelářová (2018a), Infrasound in the ionosphere from earthquakes and typhoons, *J. Atmos. Sol. Terr. Phys.*, 171, 72-82, doi:/10.1016/j.jastp.2017.07.022
- 520 Chum, J., Urbář, J., Laštovička, J., Cabrera, M. A., Liu, J.Y., Bonomi, F., Fagre, M., Fišer, J. & Mošna, Z. (2018b), Continuous Doppler sounding of the ionosphere during solar flares, *Earth, Planets and Space*, 2018, 70:198, <https://doi.org/10.1186/s40623-018-0976-4>
- Chum, J., Podolská, K., Ruzs, J., Baše, J., Tedoradze, N. (2021), Statistical investigation of gravity wave characteristics in the ionosphere. *Earth Planets Space* 73, 60, <https://doi.org/10.1186/s40623-021-01379-3>
- 525 Chum J., Šindelářová T., Koucká Knížová P., Podolská K., Ruzs J., Baše J., Nakata H., Hosokawa K., Danielides M., Schmidt C., Knez L., Liu J-Y., Molina M.G., Fagre M., Katamzi-Joseph Z., Ohya H., Omori T., Laštovička J., Obrazová Burešová D., Kouba D., Urbář J., Truhlík V. (2023), Atmospheric and ionospheric waves induced by the Hunga eruption on 15 January 2022; Doppler sounding and infrasound, *Geophys. J. Int.* (2023) 233, 1429–1443, <https://doi.org/10.1093/gji/ggac517>
- Davies K., Watts J., Zacharisen D. (1962), A study of F2-layer effects as observed with a Doppler technique. *J Geophys Res* 67:2. doi:10.1029/JZ067i002p00601
- 535 Davies K, Baker DM (1965) Ionospheric effects observed around the time of the Alaskan earthquake of March 28, 1964. *J Geophys Res* 70(9):2251-2253. doi: 10.1029/JZ070i009p02251
- Donn WL, Posmentier ES. (1964) Ground-coupled air waves from the great Alaskan earthquake. *J Geophys Res* 69:5357-536



- 540 Drob, D. P., et al. (2015), An update to the Horizontal Wind Model (HWM): The quiet time  
thermosphere, *Earth Space Sci.*, 2, 301–319, doi:10.1002/2014EA000089.
- Emmert, J.T., Drob, D.P., Picone, J.M., Siskind, D.E., Jones, M., Jr., Mlynczak, M.G. *et al.*,  
2020. NRLMSIS 2.0: a whole-atmosphere empirical model of temperature and neutral  
species densities. *Earth Space Sci.*, 8, e2020EA001321, doi:10.1029/2020EA001321.
- 545 Friis-Christensen, E., Luhr, H., Knudsen, D., & Haagmans, R. (2008). Swarm—an Earth  
observation mission investigating geospace. *Advances in Space Research*, 41(1), 210–216.  
<https://doi.org/10.1016/j.asr.2006.10.008>
- Hannawald, P., Schmidt, C., Wüst, S., and Bittner, M. (2016). A fast SWIR imager  
for observations of transient features in OH airglow. *Atmos. Meas. Tech.* 9, 1461–1472.  
550 doi:10.5194/amt-9-1461-2016
- Haralambous, H., Guerra, M., Chum, J., Verhulst, T. G. W., Barta, V., Altadill, D., et al.  
(2023). Multi-instrument observations of various ionospheric disturbances caused by the 6  
February 2023 Turkey earthquake. *Journal of Geophysical Research: Space Physics*, 128,  
e2023JA031691. <https://doi.org/10.1029/2023JA031691>
- 555 Heki, K., and J. Ping (2005), Directivity and apparent velocity of the coseismic ionospheric  
disturbances observed with a dense GPS array, *Earth Planet. Sci. Lett.*, 236, 845–855,  
doi:10.1016/j.epsl.2005.06.010.
- Jacobs JA, Watanabe T (1966) Doppler frequency changes in radio waves propagating  
through a moving ionosphere. *Radio Science* 1(3):257–264
- 560 Kikuchi T, Chum J., Tomizawa I, Kumiko K. K K, Hosokawa K, Ebihara Y, Hozumi K,  
Supnithi P (2021), Penetration of the electric fields of the geomagnetic sudden  
commencement over the globe as observed with the HF Doppler sounders and  
magnetometers, *Earth, Planets and Space*, 73:10, <https://doi.org/10.1186/s40623-020-01350-8>
- 565 Kikuchi T., Araki T., Hashimoto K. K., Ebihara Y., Tanaka T., Nishimura Y., Vichare G.,  
Sinha A. K., Chum J., Hosokawa K., Tomizawa I., Tanaka Y., Kadokura A. (2022),  
Instantaneous Achievement of the Hall and Pedersen–Cowling Current Circuits in  
Northern and Southern Hemispheres During the Geomagnetic Sudden Commencement on  
12 May 2021, *Front. Astron. Space Sci.* 9: 879314,  
570 <https://doi.org/10.3389/fspas.2022.879314>
- Laštovička, J., and J. Chum (2017), A review of results of the international ionospheric  
Doppler sounder network, *Adv. Space Res.*, 60, 1629–1643,  
<http://dx.doi.org/10.1016/j.asr.2017.01.032>
- Liu, J.Y., Chen, C.H., Lin, C.H., Tsai, H.F., Chen, C.H., Kamogawa, M., 2011. Ionospheric  
575 disturbances triggered by the 11 March 2011 M9.0 Tohoku earthquake. *J. Geophys. Res.*,  
116, <http://dx.doi.org/10.1029/2011JA016761>. A06319.



- Maruyama, T., & Shinagawa, H. (2014). Infrasonic sounds excited by seismic waves of the 2011 Tohoku-Oki earthquake as visualized in ionograms. *Journal of Geophysical Research: Space Physics*, 119(5), 4094–4108. <https://doi.org/10.1002/2013JA019707>
- 580 Otsuka, Y., Kotake, N., Tsugawa, T. *et al.* (2006), GPS detection of total electron content variations over Indonesia and Thailand following the 26 December 2004 earthquake. *Earth Planet Sp* **58**, 159–165. <https://doi.org/10.1186/BF03353373>
- Paul, K. S., Biswas, T., Haralambous, H., & Moses, M. (2026). Ionospheric disturbances induced by the 29 July 2025 Kuril-Kamchatka Earthquake: Multi - instrument
- 585 observations and analysis. *Journal of Geophysical Research: Space Physics*, 131, <https://doi.org/10.1029/2025JA034646>
- Reinisch, B. W., Huang, X., Galkin, I. A., Paznukhov, V., and Kozlov, A. (2005). Recent advances in real-time analysis of ionograms and ionospheric drift measurements with digisondes. *J. Atmos. Solar-Terrestrial Phys.* 67 (12), 1054-1062,
- 590 doi:10.1016/j.jastp.2005.01.009
- Rolland LM, Lognonné P, Munekane H (2011), Detection and modeling of Rayleigh wave induced patterns in the ionosphere. *J Geophys Res* 116: A05320. doi:10.1029/2010JA016060
- Schmidt, C., Höppner, K., Bittner, M. (2013). A ground-based spectrometer equipped with an
- 595 InGaAs array for routine observations of OH(3-1) rotational temperatures in the mesopause region. *J. Atmos. Sol. Terr. Phys.* 102, 125–139. <https://doi.org/10.1016/j.jastp.2013.05.001>.
- Schmidt, C., Dunker, T., Lichtenstern, S., Scheer, J., Wüst, S., Hoppe, U.-P., Bittner, M. (2018), Derivation of vertical wavelengths of gravity waves in the MLT-region from
- 600 multispectral airglow observations. *J. Atmos. Sol. Terr. Phys.* 173: 119-127. <https://doi.org/10.1016/j.jastp.2018.03.002>.
- Snively JB (2013) Mesospheric hydroxyl airglow signatures of acoustic and gravity waves generated by transient tropospheric forcing. *Geophys Res Lett* 40(17):4533-4537. <https://doi.org/10.1002/grl.50886>
- 605 Song, R., Hattori, K., Zhang, X. *et al.* (2025), A case study of the three-dimensional co-seismic ionospheric disturbance evolution. *Sci Rep* **15**, 42209. <https://doi.org/10.1038/s41598-025-26074-1>
- Sutcliffe PR., Poole, AWV. (1989), Ionospheric Doppler and electron velocities in the presence of ULF waves. *J Geophys Res* 94(A10):13505-
- 610 13514. <https://doi.org/10.1029/JA094iA10p13505>
- von Savigny, Ch, McDade, I.C., Eichmann, K.U., Burrows, J.P. (2012). On the dependence



- of the OH\* Meinel emission altitude on vibrational level: SCIAMACHY observations and model simulations. *Atmos. Chem. Phys.* 12 (18), 8813–8828, <https://doi.org/10.5194/acp-12-8813-2012>
- 615 Watada S, Kunugi T, Hirata K, Sugioka H, Nishida K, Sekiguchi S, Oikawa J, Tsuji Y, Kanamori H (2006) Atmospheric pressure change associated with the 2003 Tokachi-Oki earthquake. *Geophys Res Lett* 33, L24306. doi:10.1029/2006GL027967
- Wüst S, Bittner M, Espy PJ, French WJR, Mulligan FJ (2023) Hydroxyl airglow observations for investigating atmospheric dynamics: results and challenges. *Atmos Chem Phys* 23(2):1599-1618. <https://doi.org/10.5194/acp-23-1599-2023>
- 620 Wüst S., Guerra M., Chum J., Gasque L.C. (2026), Using atmospheric waves for the detection and early warning of natural hazards: a review combining results from the neutral atmosphere and the ionosphere, *Surveys in Geophysics*, <https://doi.org/10.1007/s10712-025-09909-4>
- 625 Yang, H., Hernandez-Pajares, M., Jarmolowski, W., Wielgosz, P., Vadas, S. L., Colombo, L., et al. (2022). Systematic detection of anomalous ionospheric perturbations above LEOs from GNSS POD data including possible tsunami signatures. *IEEE Transactions on Geoscience and Remote Sensing*, 60, 1–23. <https://doi.org/10.1109/TGRS.2022.3182885>
- Zettergren, M. D., & Snively, J. B. (2019). Latitude and longitude dependence of ionospheric TEC and magnetic perturbations from infrasonic acoustic waves generated by strong seismic events. *Geophysical Research Letters*, 46(3), 1132–1140. <https://doi.org/10.1029/2018GL081569>
- 630